LETTER

doi:10.1038/nature21673

Interplay between metabolic identities in the intestinal crypt supports stem cell function

Maria J. Rodríguez-Colman[1], Matthias Schewe[2], Maaike Meerlo[1], Edwin Stigter[1], Johan Gerrits[3], Mia Pras-Raves[3], Andrea Sacchetti[2], Marten Hornsveld[1], Koen C. Oost[1], Hugo J. Snippert[1], Nanda Verhoeven-Duif[3], Riccardo Fodde[2] & Boudewijn M.T. Burgering[1]

The small intestinal epithelium self-renews every four or five days. Intestinal stem cells (Lgr5$^+$ crypt base columnar cells (CBCs)) sustain this renewal and reside between terminally differentiated Paneth cells at the bottom of the intestinal crypt[1]. Whereas the signalling requirements for maintaining stem cell function and crypt homeostasis have been well studied, little is known about how metabolism contributes to epithelial homeostasis. Here we show that freshly isolated Lgr5$^+$ CBCs and Paneth cells from the mouse small intestine display different metabolic programs. Compared to Paneth cells, Lgr5$^+$ CBCs display high mitochondrial activity. Inhibition of mitochondrial activity in Lgr5$^+$ CBCs or inhibition of glycolysis in Paneth cells strongly affects stem cell function, as indicated by impaired organoid formation. In addition, Paneth cells support stem cell function by providing lactate to sustain the enhanced mitochondrial oxidative phosphorylation in the Lgr5$^+$ CBCs. Mechanistically, we show that oxidative phosphorylation stimulates p38 MAPK activation by mitochondrial reactive oxygen species signalling, thereby establishing the mature crypt phenotype. Together, our results reveal a critical role for the metabolic identity of Lgr5$^+$ CBCs and Paneth cells in supporting optimal stem cell function, and we identify mitochondria and reactive oxygen species signalling as a driving force of cellular differentiation.

In the small intestine, crypts of Lieberkühn encircle each intestinal villus. At the base of these crypts the Lgr5$^+$ crypt base columnar stem cells reside and generate transit amplifying progenitors, which migrate upwards and differentiate into enterocytes, tuft, goblet or enteroendocrine cells[1]. Paneth cells support stem cell function of Lgr5$^+$ CBCs by supplying essential factors (WNT, Delta-like 1 and epidermal growth factor). Cell metabolism has been implicated in stem cell maintenance and differentiation in some adult stem cell populations[2–5]. Recently, calorie restriction has been shown to increase Lgr5$^+$ CBCs and Paneth cell numbers[6], but otherwise the role of metabolism in the intestinal crypt homeostasis remains unknown. We analysed the metabolome of Lgr5$^+$ CBCs, Paneth cells and the remaining population of cells (CD24$^-$Lgr5$^-$) isolated from the small intestine of Lgr5–GFP mice. Principal component analysis (PCA) of liquid chromatography–tandem mass spectrometry (LC-MS/MS)-based metabolomics shows clear clustering of the metabolic profiles based on cell identity (Fig. 1a, Extended Data Fig. 1a). The pyruvate/lactate ratio, a measure of the relative contribution to cellular bioenergetics of mitochondrial respiration versus glycolysis, differed between populations, indicating increased mitochondrial activity in Lgr5$^+$ CBCs (Fig. 1b). Small intestinal organoids recapitulate *in vitro* many aspects of the intestine, including crypt structure and the interaction between Paneth cells and stem cells (reviewed in refs 7, 8). Live imaging of mitochondria and mitochondrial membrane potential (MMP), indicates increased mitochondrial activity in Lgr5$^+$ CBCs when compared to the adjacent Paneth cells (Fig. 1c, d, Extended Data Fig. 1b, c). Additionally, organoids enriched with Lgr5$^+$ CBCs[9] showed a 20% increase in respiration, supporting the notion that Lgr5$^+$ CBCs display increased mitochondrial activity (Extended Data Fig. 1d, e). Mitochondrial-derived reactive oxygen species (ROS) can contribute to cellular redox stress. Therefore, we analysed the level of mitochondrial superoxide and cytosolic ROS in organoids. Although mitochondrial superoxide is higher in Lgr5$^+$ CBCs compared to Paneth cells, cytoplasmic ROS levels do not differ between Paneth cells and CBCs (Extended Data Fig. 1f, g), indicating that higher mitochondrial activity does not necessarily result in increased redox stress in Lgr5$^+$ CBCs.

In standard medium (ENR; containing epidermal growth factor, noggin, and R-spondin 1) organoids grow as mini-guts with defined crypt domains. However, the addition of Wnt3a-conditioned medium (WENR) results in spherical organoids that lack differentiated cell types and homogeneously proliferate[10] (Fig. 2a, b). This differs from mini-gut organoids where proliferation is restricted to Lgr5$^+$ CBCs and transit amplifying cells (Fig. 2b, Extended Data Fig. 2a). Stem cell markers *Lgr5* and *Olfm4* are downregulated in spherical organoids (Fig. 2a, Extended

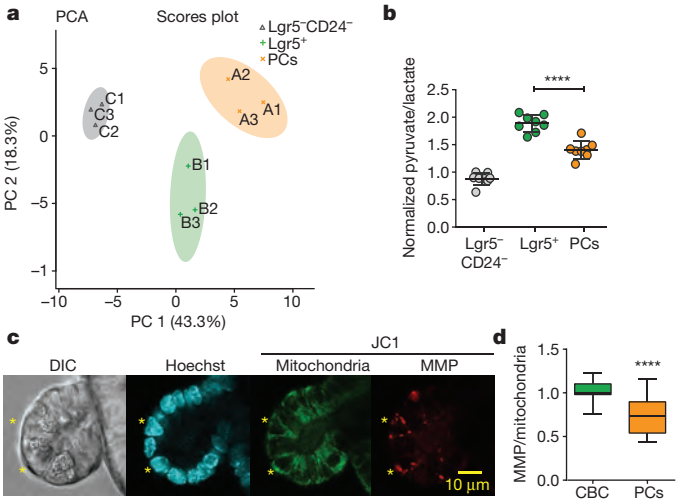

Figure 1 | Metabolic compartmentalization in the crypt. a, Lgr5$^+$ CBCs, Paneth cells (PCs) and Lgr5$^-$CD24$^-$ cells populations were obtained by FACS followed by LC-MS/MS metabolomics and PCA ($n = 3$; cells sorted from two mice were pooled for each independent measurement) **b**, Pyruvate/lactate ratio. **c**, JC-1 staining of mitochondria (green) and mitochondria with high MMP (red) in an organoid crypt. *Indicates CBCs located between Paneth cells. DIC, differential interference contrast. **d**, Quantification of JC-1 in CBCs (20) and Paneth cells (10) from 3 different organoids (one representative experiment of 3 independent ones). Graphs show mean and s.d. Two-tailed *t*-test (**b**) and Mann–Whitney test (**d**), ****$P < 0.0001$.

[1]Molecular Cancer Research, Center Molecular Medicine, University Medical Center Utrecht, Heidelberglaan 100, 3584CG Utrecht, The Netherlands. [2]Department of Pathology, Erasmus MC Cancer Institute, Erasmus University Medical Center, Rotterdam, The Netherlands. [3]Department of Genetics and Center for Molecular Medicine, Lundlaan 6, 3584 EA Utrecht, The Netherlands.

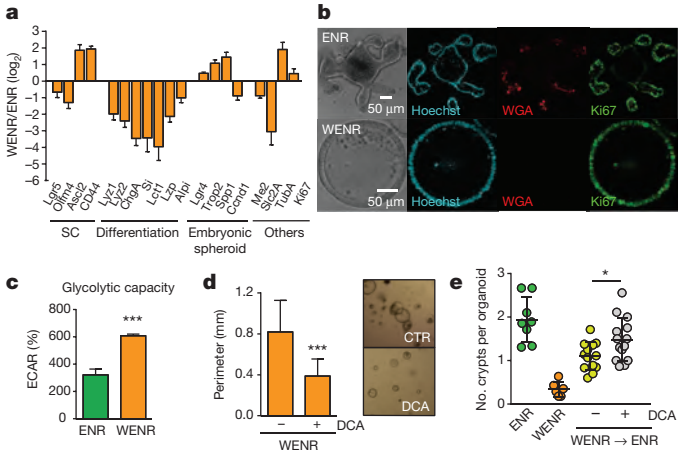

Figure 2 | Characterization of WENR organoids. a, Gene expression in WENR organoids was determined by quantitative PCR and represented as ratio relative to ENR organoids. Plotted values statistically differ from ENR condition ($n = 5$; two-tailed t-test $P < 0.05$). **b**, Representative images of immunostained mini-gut (ENR) and spherical organoids (WENR). Paneth cells and proliferative cells were detected with WGA and Ki67 antibody, respectively ($n = 3$). **c**, Glycolytic capacity was determined by glycolysis stress test (Seahorse). **d**, WENR organoids were treated with DCA and the perimeter was measured with ImageJ. **e**, Crypt formation by inhibition of glycolysis was analysed by differentiation assay adding DCA. Results show one representative experiment of $n = 5$ (**e**) and $n = 3$ (**c**, **d**). Mean and s.d. are plotted. Two-tailed t-test, $^*P < 0.05$, $^{***}P < 0.001$.

Data Fig. 2b), whereas the expression of embryonic stem cell markers (*Trop2* and *Spp1*) is increased (Fig. 2a). Remarkably, spherical WENR organoids resemble embryonic small intestine organoids, as both grow as homogenous proliferative spheres that lack differentiated cells and share a similar gene expression signature, which is distinct from adult Lgr5$^+$ CBCs[11]. Embryonic organoids can differentiate spontaneously (intestinalization) and become mini-gut organoids[11,12]. WENR organoids can reproduce this process; by removal of Wnt3a from the medium after splitting, Paneth cells and Lgr5$^+$ CBCs emerge in budding structures and crypt formation is restored[10,13,14] (Extended Data Fig. 2b, c). Thus, switching spherical organoids from WENR to ENR medium establishes a model to study differentiation preceding crypt formation.

Spherical WENR organoids display enhanced glycolytic metabolism when compared to mini-guts (Fig. 2c, Extended Data Fig. 2d, e). Accordingly, spherical organoids showed a decreased pyruvate/lactate ratio (Extended Data Fig. 2f). Inhibition of pyruvate dehydrogenase kinase 1 by dichloroacetate (DCA), and hence inhibition of glycolysis[15,16] (Extended Data Fig. 2g), resulted in reduced proliferation (Fig. 2d, Extended Data Fig. 2h). Inhibition of proliferation probably precedes the onset of differentiation. Indeed, glycolytic perturbation by addition of DCA or 2-deoxy-D-glucose enhanced the number of crypts per organoid and the expression of the Paneth cell markers *Lyz1* and *Lyz2* (Fig. 2e, Extended Data Fig. 2i–k). ATP production relies on mitochondrial oxidative phosphorylation (OXPHOS) when glycolysis is perturbed, therefore we analysed OXPHOS contribution to differentiation. Galactose, through the Leloir pathway, activates OXPHOS[17,18]. Substitution of glucose with galactose enhanced crypt formation (Extended Data Fig. 2l), suggesting that mitochondrial activation drives differentiation. In addition, mitochondrial copy number increased during differentiation (Extended Data Fig. 3a). Phenotypically, crypt formation in organoids is initiated through an increase in cell density, forming a bud-like structure, and mitochondrial activity appears increased within the initiating crypt (Fig. 3a, Extended Data Fig. 3b). Inhibition of mitochondrial OXPHOS by blocking the electron transport chain complex I or IV or ATP synthase reduced crypt formation (Extended Data Fig. 3c, d). Notably, Wnt3a enhanced the effect of blocking the electron transport chain (Extended Data Fig. 3e). Together, these results indicate that mitochondrial electron transport chain activity is required for crypt formation initiation. Increased OXPHOS activity may lead to ROS generation with consequent alteration of the cellular redox state. Glutathione is the main cellular anti-oxidant and its oxidized/reduced state in mitochondria can be analysed by the genetically encoded sensor mtGrx1–roGFP[19] (mitochondrial encoded glutaredoxin1 fused to reduction–oxidation sensitive GFP) in organoids (Extended Data Fig. 3f). Spherical organoids display throughout a homogeneous redox ratio, but following initiation of differentiation, redox state in budding areas is altered (Fig. 3b, Extended Data Fig. 3g). Thus, increased mitochondrial activity results in mitochondrial redox changes and consequent ROS signalling that may initiate differentiation and crypt formation. Indeed, exogenous antioxidants, mitoTEMPO, and to a lesser extent EUK-134, inhibited crypt formation and Paneth cell marker expression (Extended Data Fig. 3h, i). Furthermore, low concentrations of paraquat, to mimic mitochondrial ROS signalling, enhanced expression of Paneth cell markers, but did not result in a significant increase of the numbers of crypts (Extended Data Fig. 3j, k), suggesting that other functions of mitochondria (that is, ATP, metabolic intermediates) also contribute to crypt formation.

p38 MAP kinases respond to cellular redox changes[20,21]. In organoids, mitochondrial-derived ROS signals activate p38 and its activity also increases during differentiation (Extended Data Fig. 4a, b, Supplementary Fig. 1). To measure p38 activation at the cellular level, we employed the genetically encoded sensor p38KTRClover[22]. We validated p38KTRClover in organoids (Extended Data Fig. 4c) and confirmed that mitochondrial ROS activates p38 (Fig. 4a). Notably, during differentiation, p38 activity increased at budding sites and was active in in emerging Lyz-positive cells (Paneth cells) and CBCs (Fig. 4b, c). p38 activity is sustained during crypt maturation and in mature crypts, where it becomes less active towards the villi domain (Fig. 4c). Further, immunohistochemistry of mouse intestine corroborates these results and also shows increased phospho-p38 at the base of the intestinal crypt and in Paneth cells and CBCs (Fig. 4d,

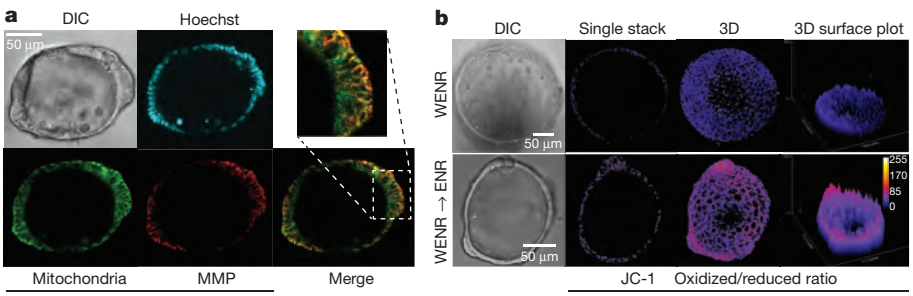

Figure 3 | Mitochondrial OXPHOS and ROS signalling drive differentiation and crypt formation. a, Representative confocal image of mitochondria and high MMP mitochondria of JC-1-stained organoids in transition to differentiation. **b**, Representative images of mitochondrial redox state analysed in mtGrx1–roGFP organoids. Images represent oxidized/reduced roGFP. One representative experiment of $n = 3$ are shown.

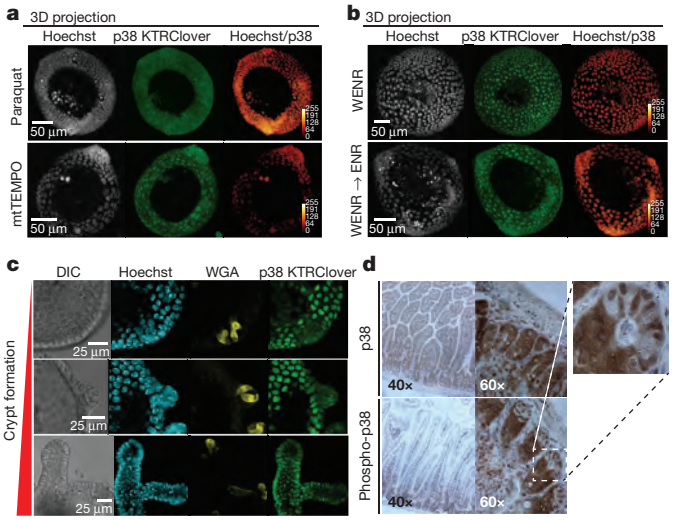

Figure 4 | p38 activity drives differentiation and crypt formation. **a**, **b**, Representative images of p38 activity as determined by confocal microscopy of p38KTRClover organoids by calculating the Hoechst/p38KTRClover ratio ($n = 5$). **c**, Detailed visualization of p38 activity at different stages of crypt formation on p38KTRClover organoids ($n = 5$). **d**, immunohistochemistry of p38 and pp38 on mouse intestinal sections.

Extended Data Fig. 4d). Inhibition of p38 activity reduced differentiation and crypt formation (Extended Data Fig. 4e, f) and thereby phenocopied mitochondrial ROS scavenging. Together, our results show that mitochondrial OXPHOS activity drives differentiation and crypt formation by a mechanism that involves p38 activation through mitochondrial ROS signalling.

Lastly, we addressed the role of metabolism in the maintenance of stem cell function. We therefore employed the organoid reconstitution assay, in which isolated Lgr5$^+$ CBCs were combined with Paneth cells to produce self-renewing organoids. This assay serves as a proxy for stem and niche cell function[6,10,23,24]. To test the relevance of metabolic compartmentalization between Lgr5$^+$ CBCs and Paneth cells, we treated either cell population with metabolic inhibitors that showed expected efficacy and did not affect cell viability (Extended Data 5a, b). Notably, Paneth cells pre-treated with inhibitors of glycolysis or glucose and lactate transporters were inefficient in supporting organoid formation upon reconstitution with Lgr5$^+$ CBCs, whereas upon treatment with OXPHOS inhibitors, Paneth cells retained their niche-supporting function (Fig. 5b). Conversely, treatment of Lgr5$^+$ CBCs with OXPHOS inhibitors clearly reduced organoid reconstitution, whereas the other inhibitors showed a mild effect (Fig. 5a). These results show that the glycolytic phenotype in Paneth cells and increased OXPHOS in Lgr5$^+$ CBCs are required in supporting both niche and stem cell function.

Lactate is the end product of glycolysis and can be back converted into pyruvate and fuel OXPHOS. We hypothesized that lactate produced by Paneth cells could provide the respiratory substrate to sustain OXPHOS in Lgr5$^+$ CBCs. Wnt ligands can substitute for Paneth cells in supporting *ex vivo* Lgr5$^+$ CBCs to form organoids[6,10,23]. We therefore repeated reconstitution assays, replacing Paneth cell function with Wnt3a and either glucose or lactate. Indeed, lactate strongly enhanced the ability of Lgr5$^+$ CBCs to establish organoids (Fig. 5c). Thus, besides Wnt3a, glycolysis towards lactate in Paneth cells establishes the stem cell niche. Next, we analysed the effects of replacing lactate by pyruvate, inhibition of pyruvate transport into mitochondria, and inhibition of ROS and p38 signalling. Our results indicate that in Lgr5$^+$ CBCs, lactate is converted into pyruvate to fuel mitochondrial OXPHOS, leading to ROS signalling and activation of p38 and differentiation (Fig. 5d, e, Extended Data Fig. 5c–g). Together, our results reveal the existence of metabolic compartmentalization in the intestinal crypt in which Paneth cells support Lgr5$^+$ CBC oxidative metabolism, constituting a metabolic niche that provides optimal stem cell function (Fig. 5f).

Several studies have indicated a role for metabolism in stem cell function, but a clear understanding has been lacking[2–5]. Here, we report that a metabolic transition towards mitochondrial OXPHOS is required to drive differentiation in an organoid model representing the development of the intestinal crypt *in vivo*. Importantly, this metabolic transition towards OXPHOS and consequent p38 activation is maintained in adult Lgr5$^+$ CBCs and ultimately regulates stem cell function by self-renewal and differentiation capacity. In agreement with our results, deregulation of mitochondrial COX1 in *Drosophila*

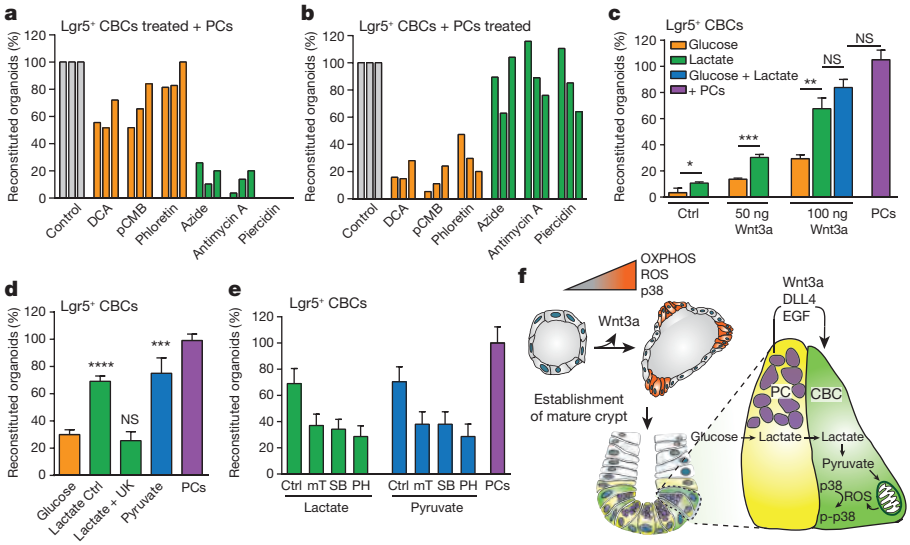

Figure 5 | Metabolic regulation of Lgr5$^+$ CBC stem cell function. **a**, **b**, OXPHOS in Lgr5$^+$ CBCs (**a**) and glycolysis in Paneth cells (**b**) are required for stem cell function. Organoid reconstitution efficiency was determined in Lgr5$^+$ CBCs or Paneth cells were treated with glycolysis (orange) or OXPHOS inhibitors (green) before combining and plating on matrigel ($n = 3$). **c**, Single Lgr5$^+$ CBCs were plated in ENR medium supplemented as indicated and organoid reconstitution efficiency was determined ($n = 6$). **d**, **e**, Organoid reconstitution efficiency was assessed by plating single Lgr5$^+$ CBCs in medium supplemented with 100 ng Wnt3a and the indicated compounds ($n = 6$). Ctrl, control; mT, mitoTEMPO; PH, PH-797804; SB, SB203580; UK, UK-5099. Average and s.d. are shown. Two-tailed *t*-test, $*P < 0.05$, $**P < 0.01$, $***P < 0.001$, NS, not significant. **f**, Schematic representation of the main findings in this work. p-p38, phospho-p38.

melanogaster leads to loss of CBCs and decreased number of crypts[25]. Also, conditional p38α-knockout mice show altered epithelial homeostasis in colon and small intestine[26]. Studies on ROS and stem cell fate have focused mostly on ROS as a causal mechanism for DNA damage rather than on its role in signalling (discussed in ref. 27). However, mitochondrial-derived ROS does not inevitably result in increased DNA damage[28,29], and our results indicate that increased OXPHOS in Lgr5$^+$ CBCs generates ROS signalling rather than stress. Interestingly, gene expression profiling suggests that there is similarity between normal Lgr5$^+$ CBCs and colon cancer stem cells[25], and this could also be true of their metabolism. Indeed, increased mitochondrial metabolism in cancer stem cells has been previously reported[30]. Thus, whereas the bulk of cancer cells adopt a 'Warburg metabolism', the minor population of cancer stem cells may rely on OXPHOS. Therefore, targeting mitochondria may provide therapeutic benefit in eradicating cancer stem cells, as opposed to other strategies that target the bulk of a tumour.

Online Content Methods, along with any additional Extended Data display items and Source Data, are available in the online version of the paper; references unique to these sections appear only in the online paper.

Received 9 May 2016; accepted 30 January 2017.
Published online 8 March 2017.

1. Barker, N. *et al.* Identification of stem cells in small intestine and colon by marker gene *Lgr5*. *Nature* **449,** 1003–1007 (2007).
2. Zhang, J. *et al.* UCP2 regulates energy metabolism and differentiation potential of human pluripotent stem cells. *EMBO J.* **30,** 4860–4873 (2011).
3. Owusu-Ansah, E. & Banerjee, U. Reactive oxygen species prime *Drosophila* haematopoietic progenitors for differentiation. *Nature* **461,** 537–541 (2009).
4. Tormos, K. V. *et al.* Mitochondrial complex III ROS regulate adipocyte differentiation. *Cell Metab.* **14,** 537–544 (2011).
5. Hamanaka, R. B. *et al.* Mitochondrial reactive oxygen species promote epidermal differentiation and hair follicle development. *Sci. Signal.* **6,** ra8 (2013).
6. Yilmaz, Ö. H. *et al.* mTORC1 in the Paneth cell niche couples intestinal stem-cell function to calorie intake. *Nature* **486,** 490–495 (2012).
7. Yin, X. *et al.* Engineering stem cell organoids. *Cell Stem Cell* **18,** 25–38 (2016).
8. Barker, N. Adult intestinal stem cells: critical drivers of epithelial homeostasis and regeneration. *Nat. Rev. Mol. Cell Biol.* **15,** 19–33 (2014).
9. Yin, X. *et al.* Niche-independent high-purity cultures of Lgr5$^+$ intestinal stem cells and their progeny. *Nat. Methods* **11,** 106–112 (2014).
10. Sato, T. *et al.* Paneth cells constitute the niche for Lgr5 stem cells in intestinal crypts. *Nature* **469,** 415–418 (2011).
11. Mustata, R. C. *et al.* Identification of Lgr5-independent spheroid-generating progenitors of the mouse fetal intestinal epithelium. *Cell Reports* **5,** 421–432 (2013).
12. Fordham, R. P. *et al.* Transplantation of expanded fetal intestinal progenitors contributes to colon regeneration after injury. *Cell Stem Cell* **13,** 734–744 (2013).
13. Sato, T. & Clevers, H. Growing self-organizing mini-guts from a single intestinal stem cell: mechanism and applications. *Science* **340,** 1190–1194 (2013).
14. Sato, T. *et al.* Long-term expansion of epithelial organoids from human colon, adenoma, adenocarcinoma, and Barrett's epithelium. *Gastroenterology* **141,** 1762–1772 (2011).
15. Kankotia, S. & Stacpoole, P. W. Dichloroacetate and cancer: new home for an orphan drug? *Biochim. Biophys. Acta* **1846,** 617–629 (2014).
16. Michelakis, E. D., Webster, L. & Mackey, J. R. Dichloroacetate (DCA) as a potential metabolic-targeting therapy for cancer. *Br. J. Cancer* **99,** 989–994 (2008).
17. Zhdanov, A. V., Waters, A. H., Golubeva, A. V., Dmitriev, R. I. & Papkovsky, D. B. Availability of the key metabolic substrates dictates the respiratory response of cancer cells to the mitochondrial uncoupling. *Biochim. Biophys. Acta* **1837,** 51–62 (2014).
18. Aguer, C. *et al.* Galactose enhances oxidative metabolism and reveals mitochondrial dysfunction in human primary muscle cells. *PLoS One* **6,** e28536 (2011).
19. Gutscher, M. *et al.* Real-time imaging of the intracellular glutathione redox potential. *Nat. Methods* **5,** 553–559 (2008).
20. Tormos, A. M., Taléns-Visconti, R., Nebreda, A. R. & Sastre, J. p38 MAPK: a dual role in hepatocyte proliferation through reactive oxygen species. *Free Radic. Res.* **47,** 905–916 (2013).
21. Wagner, E. F. & Nebreda, A. R. Signal integration by JNK and p38 MAPK pathways in cancer development. *Nat. Rev. Cancer* **9,** 537–549 (2009).
22. Regot, S., Hughey, J. J., Bajar, B. T., Carrasco, S. & Covert, M. W. High-sensitivity measurements of multiple kinase activities in live single cells. *Cell* **157,** 1724–1734 (2014).
23. Sato, T. *et al.* Single Lgr5 stem cells build crypt-villus structures *in vitro* without a mesenchymal niche. *Nature* **459,** 262–265 (2009).
24. Schewe, M. *et al.* Secreted phospholipases A2 are intestinal stem cell niche factors with distinct roles in homeostasis, inflammation, and cancer. *Cell Stem Cell* **19,** 38–51 (2016).
25. Merlos-Suárez, A. *et al.* The intestinal stem cell signature identifies colorectal cancer stem cells and predicts disease relapse. *Cell Stem Cell* **8,** 511–524 (2011).
26. Otsuka, M. *et al.* Distinct effects of p38α deletion in myeloid lineage and gut epithelia in mouse models of inflammatory bowel disease. *Gastroenterology* **138,** 1255–1265 (2010).
27. Liang, R. & Ghaffari, S. Stem cells, redox signaling, and stem cell aging. *Antioxid. Redox Signal.* **20,** 1902–1916 (2014).
28. Hoffmann, S., Spitkovsky, D., Radicella, J. P., Epe, B. & Wiesner, R. J. Reactive oxygen species derived from the mitochondrial respiratory chain are not responsible for the basal levels of oxidative base modifications observed in nuclear DNA of Mammalian cells. *Free Radic. Biol. Med.* **36,** 765–773 (2004).
29. Cleaver, J. E. *et al.* Mitochondrial reactive oxygen species are scavenged by Cockayne syndrome B protein in human fibroblasts without nuclear DNA damage. *Proc. Natl Acad. Sci. USA* **111,** 13487–13492 (2014).
30. Song, I. S. *et al.* FOXM1-induced PRX3 regulates stemness and survival of colon cancer cells via maintenance of mitochondrial function. *Gastroenterology* **149,** 1006–1016 (2015).

Supplementary Information is available in the online version of the paper.

Acknowledgements This work was financially supported by CGC.nl (M.J.R.-C., H.J.S.), Utrecht Life Sciences (M.M.), Dutch Cancer Society ((KWF), EMCR 2012-5473 (M.S.), and UU 2013-6070 (K.C.O.)) and from the Netherlands Institute of Regenerative Medicine (R.F.). We thank H. Bos, T. Dansen and S. van Mil for helpful discussions and proofreading; F. de Sauvage (Genentech) for providing DTR–LGR5–GFP mice; T. Dick (DKFZ) for mtGrx1–roGFP and I. Verlaan (UMC Utrecht) for R-spondin/Wnt3a-conditioned medium.

Author Contributions M.J.R.-C. and B.M.T.B. conceived the project, designed and performed experiments and wrote the manuscript; M.S. designed and performed organoid reconstitution experiments; M.M. performed experiments; E.S. and J.G. performed metabolic measurements. M.P.-R. and N.V.-D. performed metabolic data analysis. A.S. performed FACS of intestinal cells. M.H. performed p38 IHC. K.C.O. and H.J.S. provided organoid cultures, and H.J.S. co-wrote the manuscript. R.F. designed experiments and co-wrote the manuscript.

Author Information Reprints and permissions information is available at www.nature.com/reprints. The authors declare no competing financial interests. Readers are welcome to comment on the online version of the paper. Publisher's note: Springer Nature remains neutral with regard to jurisdictional claims in published maps and institutional affiliations. Correspondence and requests for materials should be addressed to B.M.B. (b.m.t.burgering@umcutrecht.nl).

Reviewer Information *Nature* thanks T. Sato, A. Schulze and the other anonymous reviewer(s) for their contribution to the peer review of this work.

METHODS

Data reporting. No statistical methods were used to predetermine sample size. The experiments were not randomized and the investigators were not blinded to allocation during experiments and outcome assessment.

Organoid culture. Small intestinal organoids were derived from isolated crypts collected from the entire length of the small intestine of wild-type, LGR5–GFP or DTR–LGR5–GFP mice as described ref. in 14. The basic culture medium (ENR) contained advanced DMEM/F12 supplemented with penicillin/streptomycin, 10 mM HEPES, 1× Glutamax, 1× B27 (all from Life Technologies) and 1 mM N-acetylcysteine (Sigma) that was supplemented with murine recombinant epidermal growth factor (Peprotech), R-spondin1-CM (5% v/v) and noggin-CM (10% v/v). WENR medium was prepared with ENR medium supplemented with R-spondin1-CM (20% v/v) and 50% Wnt3a-CM (conditioned medium) (v/v). A mycoplasma-free status was confirmed routinely.

Lentiviral infection. mtGrx1–roGFP in pLPCX redox sensor was cloned into a lentiviral vector under the control of *Hef1* promoter and with puromycin resistance cassette. pLentiPGK Puro DEST p38KTRClover was purchased in Addgene. p38KTRClover[30] facilitates tracking of p38 activity by live imaging of nuclear (inactive) and cytoplasmic (active) localization of the GFP sensor. mtGrx1–roGFP in pLPCX was a gift of T. Dick (Cancer Research Center, Heidelberg, Germany). The genetically encoded sensor mtGrx1–roGFP allows for ratiometric quantification in mitochondria of oxidized/reduced glutathione by excitation with 405 and 488 nm, respectively, and emission in the green channel[26]. Both genetic encoded sensors were introduced in organoids by lentiviral infection according to ref. 31.

Differentiation assay. Organoids were grown in WENR medium until crypts were no longer visible (approximately 7 days per one passage). WENR spherical organoids were split up and plated in either WENR or ENR medium. Galactose and glucose media were prepared using advanced F12 glucose free medium and supplemented with either galactose or glucose to a final concentration of 15 mM and used as regular F12 to prepare ENR medium. Compounds were added along with the medium directly after plating, with the exception of EUK134, mitoTEMPO, paraquat and antimycinA, which were added 14–16 h after plating. EUK134 mimics catalase and superoxide dismutase activity and, in this way, scavenges ROS in the cytosol, and mitoTEMPO is a scavenger of mitochondrial superoxide[32]. DCA concentration was 15 mM. Pictures were taken after 48 or 72 h after treatment. All compounds were purchased from Sigma. The number of organoids and crypts were blindly counted with the cell counter (ImageJ plugin) and crypt formation was scored as the number of crypts divided by the number of organoids per picture. For each condition, a minimum of six pictures with approximately 6–10 organoids per picture were counted (see Extended Data Fig. 2j for an example). Statistical analyses were performed using Graphpad Prism 6. For crypt formation assays, an independent experiment (*n*) refers to independent splitting, plating and treatment of organoids performed on different days.

DNA and RNA extraction and qPCR. Organoids were washed once with cold PBS and collected in RLT buffer. RNA was extracted with the RNeasy kit (Qiagen), with on-column DNase treatment (Qiagen), according to the manufacturer's instructions. RNA was reverse-transcribed with oligodT primers and the CBCript cDNA synthesis kit (Biorad). For DNA extraction, organoids were washed once with cold PBS and DNA was extracted with the QIAamp DNA Micro Kit (Qiagen). DNA was used as a template to amplify nuclear and mitochondria-encoded genes. In both cases, qPCR was performed with FastStart SYBR Green Master mix (Roche). Relative gene expression was calculated using the C_t method by normalization to HNRNPA1 and CycA. Statistics were done with Graphpad Prism 6. Primer sequences: *Glut1* forward (5′-GCAGTTCGGCTATAACACT-3′), *Glut1* reverse (5′-GGTGGTTCCATGTTTGATTG-3′); *Hk1* forward (5′-AAGGATGACCAAGTCAAAAAGATTG-3′), *Hk1* reverse (5′-CGGGAGAGGCCATTCTTCATC-3′); *Mct1* forward (5′-GATGGACCTCATTGGACCCC-3′), *Mct1* reverse (5′-GAGGCGGCCTAAAAGTGGT-3′); *Hnrnpa1* forward (5′-TGACAGCTATAACAACGGAG-3′), *Hnrnpa1* reverse (5′-AAAGTTTCCTCCCTTCATCG-3′); *Pbgd* forward (5′-CCTCGACTCTGCTTCGTCTG-3′), *Pbgd* reverse (5′-CACAGACCACAAATCCATGA-3′); *Tuba1a* forward (5′-AGGATTATGAGGAGGTTGGT-3′), *Tuba1a* forward (5′-ATAAACATCCCTGTGGAAGC-3′); *Ppia* forward (5′-ACTGAATGGCTGGATGGCAA-3′), *Ppia* reverse (5′-CAAAACGCTCCATGGCTTCC-3′); *Lyz1* forward (5′-CGTTGTGAGTTGGCCAGAA-3′); *Lyz1* reverse (5′-GCTAAACACACCCAGTCAGC-3′); *Lyz2* forward 2 (5′-TGAACGTTGTGAGTTTGCCA-3′), *Lyz2* reverse (5′-TGAGCTAAACACACCCAGTCG-3′); *Ki67* forward (5′-CCTTTGCTGTCCCCGAAGA-3′), *Ki67* reverse (5′-GGCTTCTCATCTGTTGCTTCCT-3′); *Slc2a* forward (GLUT2) (5′-ATCGCTCCAACCACACTCAG-3′), *Slc2a* reverse (5′-GCTGAGGCCAGCAATCTGAC-3′); *Olfm4* forward (5′-TGAAGGAGATGCAAAAACTGG-3′), *Olfm4* reverse (5′-CTCCAGCTTCTCTACCAAGAGG-3′); *Me2* forward (5′-AGGCGTCCGGGGAGAG-3′), *Me2* reverse (5′-ATGAGTGGCTTGCCCTTCTC-3′); *Alpi* forward (5′-AACTCACCTCATGGGCCTCTT-3′), *Alpi* reverse (5′-GGGTTTCGGTTGGCATCATA-3′); *Lct* forward (5′-CGTCTGCTTCCTATCAGGTTGAA-3′), *Lct* reverse (5′-GTGGGAAAATGTGTCCCAGATACT-3′); *Lgr5* forward (5′-GTTCAAGATGAGCGGGACCT-3′), *Lgr5* reverse (5′-ATAGGTGCTCACAGGGCTTG-3′); *Pkm* forward (5′-ATGCAGCACCTGATAGCTCG-3′), *Pkm* reverse (5′-AGGTCTGTGGAGTGACTGGA-3′). Sequences of primers for *Ascl2*, *Cd44*, *Chga*, Si, LZP, *Lgr4*, *Trop2*, *Spp1* and CCND1 were obtained from ref. 11.

Protein lysates and western blot. Organoids were washed once with cold PBS and collected in cell recovery solution (Corning) according to the manufacturer's instructions. Total proteins were collected by direct lysis of organoids in Laemli sample buffer. Proteins were run in SDS–PAGE and transferred to Polyscreen PVDF transfer membranes (PerkinElmer). Antibodies used in this work: anti-GAPDH (Millipore), P38 antibody (Biolabs 9212); phospho-p38 (Cell Signaling CS9215); GAPDH (Millipore MAB374); Ki67 (Abcam ab15580); lysozyme (DAKO A0099), phospho-p38 MAPK (Thr180/Tyr182) (9211S, Cell Signaling), phospho-p38 MAPK (Thr180/Tyr182) (4511S, Cell Signaling).

Immunostaining, live imaging in organoids and immunohistochemistry. Organoids were plated in 4-well round Cellview plates. Samples were fixed with 4% paraformaldehyde (PFA) for 45 minutes at 4 °C. After fixation organoids were washed with cold PBS and permeabilized with PBS buffer containing 10% DMSO, 2% Triton and 10 g l^{-1} BSA. Antibody incubation was performed in the same buffer; anti-Ki67 (Abcam), rabbit anti-lysozyme (Dako). Fluorescence was detected using anti-rabbit Alexa Fluor 488 antibody. Paneth cells were also stained with wheat germ agglutinin (WGA) and DNA was stained with Hoechst (both Molecular Probes). Images were captured using a SP8 confocal microscope (Leica Microsystems). For live imaging, organoids were stained with the following probes; JC-1 (T3168), MitoTracker Deep Red FM (M22426), Tetramethylrhodamine (TMRM, T668), CellRox (C10448), MitoSOX (M36008). JC-1 dye accumulates in mitochondria; it exists as a monomer at low concentrations and yields green fluorescence. The dye forms J-aggregates at high mitochonrial membrane potential and the emission shifts to red. The ratio of green to red fluorescence is dependent only on the membrane. All probes were applied following manufacturer recommendations and were purchased from Thermo Fisher. Imaging of mtGrx1–roGFP (Fig. 3b, Extended Data Fig. 3g) was performed in 3 independent experiments and 17 organoids were analysed. Data analysis was performed according to ref. 33. Imaging of p38KTRClover (Fig. 4) was performed in 4 independent experiments and 24 organoids were analysed. Additionally, p38KTRClover organoids were treated with 1 mM mitoTEMPO overnight or 7.5 mM parquat for 90 min (Fig. 4a) and then imaged. Experiments were performed twice with 2 technical replicates in each and 30 organoids were analysed. The ratios Hoechst/Clover was considered as a measurement of p38 activity and is represented in Real Glow scale (ImageJ). ImageJ was used for all imaging analysis. For immunohistochemistry, fresh mouse intestine of one mouse was fixed in 4% formaldehyde for 24 h followed by dehydration in 70% ethanol and embedding in paraffin. Rehydrated slides were blocked for endogenous peroxidase activity in phosphate buffer (pH 5.8) containing 1.5% hydrogen peroxide. For antigen retrieval, samples were cooked for 20 min in 10 mM citrate buffer (pH 6) in a microwave. Primary and secondary horseradish-peroxidase-conjugated antibodies were incubated overnight or 1 h at 4 °C, respectively. Staining of slides was performed using diaminobenzidine and haematoxylin. For imaging, independent experiments (*n*) refer to the number of independent stainings performed and imaged on different days.

Metabolomics. Cells were sorted by FACS from intestinal crypts of mice[6]. To reach the minimal amount for analysis, cells sorted from two mice were pooled for each independent measurement, so 6 mice were used for $n = 3$. LC/MS was performed on the 3 independent samples and each sample was measured 3 times. Direct infusion mass spectrometry (DI-MS) metabolomics was performed on the 3 independent samples with 3 technical replicates measured 3 times each leading to a total of 9 measurements per group. Cells were sorted by FACS and collected directly in ice-cold methanol. After homogenization, the extracts were diluted in water and internal standards in methanol for DI-MS. Direct infusion was performed using chip-based infusion (400 nozzles, nominal internal Ø 5 μm) on the TriVersa NanoMate (Advion). High resolution mass spectrometry (140,000) was performed using a Q-ExactivePlus (Thermo Scientific GmbH) using a scan range of m/z 70 to 600 in positive and negative modes. Besides mass calibration of the instrument, internal lock masses were used for high mass accuracy. Cells were collected in biological triplicates. Cell extracts were diluted (1:1 v/v) using 70 μl stable isotopes solution in methanol (NSK-A-amino acids and NSK-B-free carnitine and acylcarnitine reference standards (Cambridge Isotope Laboratories). After dilution with 60 μl 0.3% formic acid, samples were filtered using a preconditioned (with methanol) 96-well filter plate (Acro prep, 0.2 μm GHP, NTRL, 1 ml well; Pall Corporation). The sample filtrate was collected using cleaned

96-well plate (Advion). A volume of 13 μl was infused into the DI-HRMS system in triplicate (technical replicates). RAW data files were converted to mzXML format using MSConvert[34]. The data were processed using an in-house-developed untargeted metabolomics pipeline written in the R programming language (http://www.r-project.org). First, the mzXML files were converted to readable format by the XCMS package[35]. For every sample, peak finding was performed and peaks with the same *m*/*z* (within 0.5 × full width at half maximum) were grouped over different samples. Peak groups that were not present in three out of three technical replicates in at least one biological sample were discarded. The intensities of the technical replicates were averaged. Peak groups were identified using all entries in the HMDB, including their most likely adducts (Na^+, K^+, $NH4^+$ in positive mode and Cl^- and formate in negative mode) and isotopes, using an accuracy of 3 p.p.m. or better. For LC-MS/MS analysis, 200 μl of the methanol extract was evaporated to dryness after the addition of internal standards. The residue was dissolved in 100 μl 10% acetonitrile in ultrapure water of which 5 μl was injected for analysis. Analysis was conducted with a Thermo Scientific Acella UHPLC system and an Acquity BEH C-8 column (1 × 150 mm, 1.7 μm). The column outlet was coupled to a Thermo Scientific Orbitrap XL equipped with an electrospray ion source operated in either negative or positive mode. The system was operated at a flow rate of 150 μl min^{-1} and 40 °C. The mobile phases consisted of 6.5 mM ammonium carbonate pH 8 (solvent A), and 6.5 mM ammonium carbonate in methanol (solvent B) in negative mode. For positive mode analysis the solvents were 0.1% formic acid in ultrapure water and 0.1% formic acid in methanol, respectively. A 10-min linear gradient of 0–100% B was started 3 min after the injection of the sample. The system was kept at 100% B for the next 4 min, after which the system returned to its starting situation. Total runtime was 22 min. All acquired MS-data was searched against available databases. Statistics and analysis was performed on replicates (LC-MS/MS) and on replicates and technical replicates (DI-MS). PCA analyses were performed with http://www.metaboanalyst.ca (ref. 36).

Bioenergetics. Seahorse Bioscience XFe24 Analyzer was used to measure extracellular acidification rates (ECAR) in mpH (milli pH) per min and oxygen consumption rates (OCR) in pmol O_2 per min. Organoids were seeded in 3 μl matrigel per well in XF24 cell culture microplates (Seahorse Bioscience). 1 h before the measurements, culture medium was replaced and the plate was incubated for 60 min at 37 °C. For the mitochondrial stress test, culture medium was replaced by Seahorse XF Base medium (Seahorse Bioscience), supplemented with 20 mM glucose (Sigma-Aldrich), 2 mM L-glutamine (Sigma-Aldrich), 5 mM pyruvate (Sigma-Aldrich) and 0.56 μl NaOH (1 M). During the test, 5 μM oligomycin, 2 μM FCCP and 1 μM of Rotenone and Antimycin A (all Sigma-Aldrich) were injected to each well after 18, 45 and 63 min, respectively. For the glycolysis stress test, culture medium was replaced by Seahorse XF Base medium, supplemented with 2 mM L-glutamine and 0.52 μl ml^{-1} NaOH (1 M). During the test 10 mM glucose, 5 μM oligomycin and 100 mM 2-deoxyglucose (Sigma-Aldrich) were injected to each well after 18, 36 and 65 min, respectively. After injections, measurements of 2 min were performed in triplicate, preceded by 4 min of mixture time. The first measurements after oligomycin injections were preceded by 5 min mixture time, followed by 8 min waiting time for the mitochondrial stress test and 5 min mixture time followed by 10 min waiting time for the glycolysis stress test.

Reconstitution assays. Reconstitution of *Lgr5*-EGFP^{hi} stem cells (purity >99%) with Paneth cells (CD24^{hi}SSC^{hi}; purity >98%) was performed by pelleting sorted cells at 300*g* for 5 min in Eppendorf LoBind Tubes, and by co-incubating them for 15 min at room temperature as previously described[14]. *Lgr5*-EGFP^{hi} stem cells were co-incubated with Paneth cells in equal numbers as previously described[24]. Incubation with 20 mM DCA, 100 μM pCMB, 50 μM Floretin, 50 μM Azide, 200 μM Antimycin A (all purchased in Sigma) was performed for 2 h on ice. Cells were then pelleted at 300*g* for 5 min and washed twice with ENR medium and pelleted again at 300*g*. Cells were then co-incubated for 15 min and plated as previously described. Organoids grown from single *Lgr5*-EGFP^{hi} stem cells with lactate or glucose were performed in ENR medium (base medium SILAC Advanced DMEM/F12 supplemented with arginine and lysine) supplemented with 17.5 mM glucose, Na-pyruvate or lactate where indicated. Recombinant Wnt3a (R&D systems) was used where indicated at 50 μg ml^{-1} and 100 μg ml^{-1} to promote organoid formation from single *Lgr5*-EGFP^{hi} stem cells. Where indicated cells were treated with 0.5 mM mitoTEMPO, 5 μM EUK5099, 2 μM php7879 or 5 μM SB202190. Organoid number was counted at day 5 and after counting 5 mM glucose was added to all non-glucose conditions to allow crypt formation. Pictures of organoids for crypt counting were taken at day 12. A total of 35 organoids were counted per condition. Each independent experiment refers to mice intestinal crypt isolation, FACS sorting and treatments performed on different days.

Animal experiments. Experiments involving live mice (generation of organoids) were performed in compliance with local and national ethical regulations and codes (DEC, Dier Experimenteel Commissie).

Data availability. Source Data are provided for all figures with the online version of the paper, excluding mass-spectrometry metabolomics data, which is available from the corresponding author upon reasonable request.

31. Van Lidth de Jeude, J. F., Vermeulen, J. L., Montenegro-Miranda, P. S., Van den Brink, G. R. & Heijmans, J. A protocol for lentiviral transduction and downstream analysis of intestinal organoids. *J. Vis. Exp.* http://dx.doi.org/10.3791/52531 (2015).
32. Baker, K. *et al.* Synthetic combined superoxide dismutase/catalase mimetics are protective as a delayed treatment in a rat stroke model: a key role for reactive oxygen species in ischemic brain injury. *J. Pharmacol. Exp. Ther.* **284,** 215–221 (1998).
33. Morgan, B., Sobotta, M. C. & Dick, T. P. Measuring E_{GSH} and H_2O_2 with roGFP2-based redox probes. *Free Radic. Biol. Med.* **51,** 1943–1951 (2011).
34. Chambers, M. C., Song, K. H. & Schneider, D. S. *Listeria monocytogenes* infection causes metabolic shifts in *Drosophila melanogaster*. *PLoS One* **7,** e50679 (2012).
35. Smith, C. A., Want, E. J., O'Maille, G., Abagyan, R. & Siuzdak, G. XCMS: processing mass spectrometry data for metabolite profiling using nonlinear peak alignment, matching, and identification. *Anal. Chem.* **78,** 779–787 (2006).
36. Xia, J., Sinelnikov, I. V., Han, B. & Wishart, D. S. MetaboAnalyst 3.0—making metabolomics more meaningful. *Nucleic Acids Res.* **43,** W251–W257 (2015).

a

ANOVA	p.value	FDR	Post-hoc tests
2-Oxobutanoate	1.96E-07	1.41E-05	Lgr5$^+$- Neg.; Paneth - Neg.
Indole-3-acetaldehyde	2.39E-05	0.00086	Neg. - Lgr5$^+$; Paneth - Neg.; Paneth - Lgr5$^+$
2-Aminoadipate	0.000159	0.00326	Neg. - Lgr5$^+$; Neg. - Paneth
(iso)Leucine	0.000223	0.00326	Neg. - Lgr5$^+$; Neg. - Paneth; Lgr5$^+$ - Paneth
Glucosamine	0.000271	0.00326	Neg. - Lgr5$^+$; Neg. - Paneth; Lgr5$^+$ - Paneth
Hypoxanthine	0.000283	0.00326	Neg. - Lgr5$^+$; Neg. - Paneth; Lgr5$^+$- Paneth
Palmitoylcarnitine	0.000317	0.00326	Paneth - Neg.; Paneth - Lgr5$^+$
4-Methylene-L-glutamate	0.000552	0.00497	Neg. - Paneth; Lgr5$^+$ - Paneth
Tryptophan	0.000886	0.00709	Neg. - Paneth; Lgr 5$^+$- Paneth
2,6 dimethylheptanoyl carnitine	0.001003	0.00722	Lgr5$^+$- Neg.; Paneth - Neg.; Lgr5$^+$ Paneth

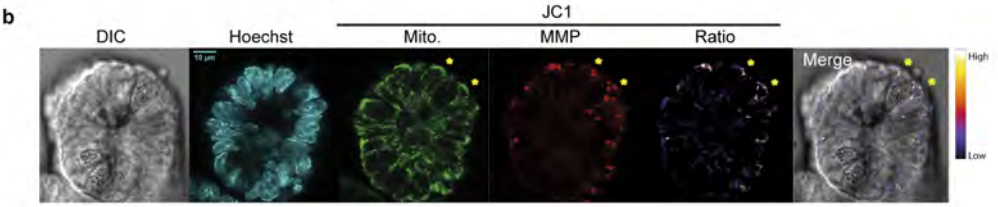

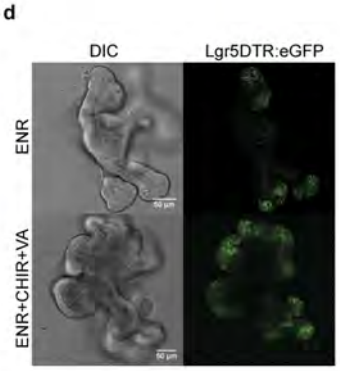

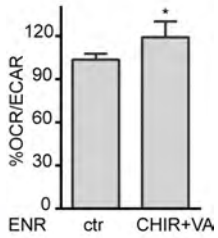

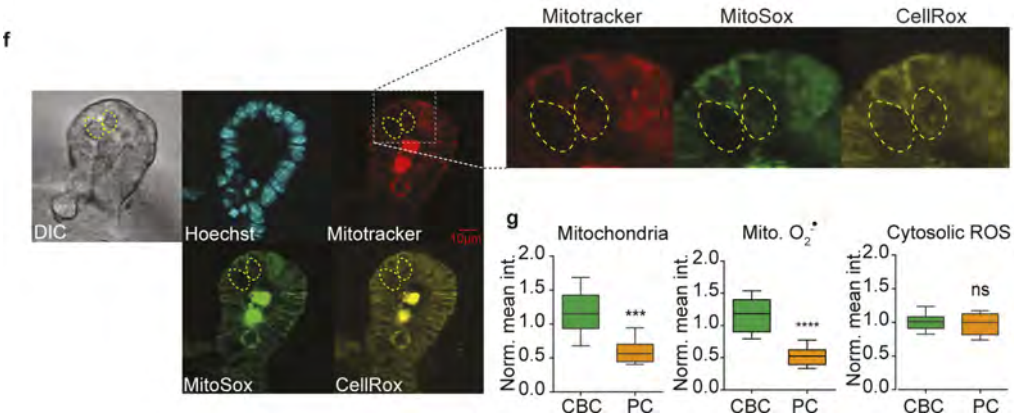

Extended Data Figure 1 | Metabolic compartmentalization and mitochondria and redox state in the crypt. a, Top 10 most different metabolites between Lgr5$^+$ CBCs, Paneth cells (PCs) and all other differentiated cell types ('Neg.'). *P* value and false discovery rate (FDR) refer to the significance, and post hoc tests indicate the groups being compared. Results were obtained by analysis with http://metaboanalyst.ca. **b**, Live confocal microscopy of organoid crypts. All mitochondria (green) and high MMP (red) was determined by JC-1 staining. MMP/mitochondria ratio is represented in fire intensity scale (ImageJ). **c**, Live imaging of Lgr5–GFP-derived organoid stained with Mitotracker Deep-Red confirmed increased mitochondria in Lgr5$^+$ CBCs. In both cases Hoechst was used to stain nuclei. Asterisks indicate stem cells in between Paneth cells ($n = 1$). **d**, Representative images of DTR–Lgr5–eGFP organoids grown in ENR medium or ENR medium supplemented with CHIR99021 (3 μM) and valproic acid (2 mM) during 72 h. **e**, Mitochondrial respiration/glycolysis (basal) was measured during mitochondrial stress test using Seahorse technology. Organoids were grown in ENR medium and after 24 h CHIR99021 and valproic acid were added to half of the plate during 72 h before running the assay. Graph represents mean and s.d. of 6 independent Seahorse experiments. Two-tailed *t*-test, $^*P < 0.05$. **f**, ROS in the crypt was stained with CellRox (cytosolic ROS), MitoSOX (mitochondrial superoxide) and Mitotracker (mitochondria). Dashed yellow regions indicate Paneth cells. **g**, Quantification of ROS in CBCs (16) and Paneth cells (6) from 3 organoids. One representative experiment of 2 independent ones. Graphs show mean and s.d. Two tailed *t*-test, $^{****}P < 0.0001$, NS, not significant.

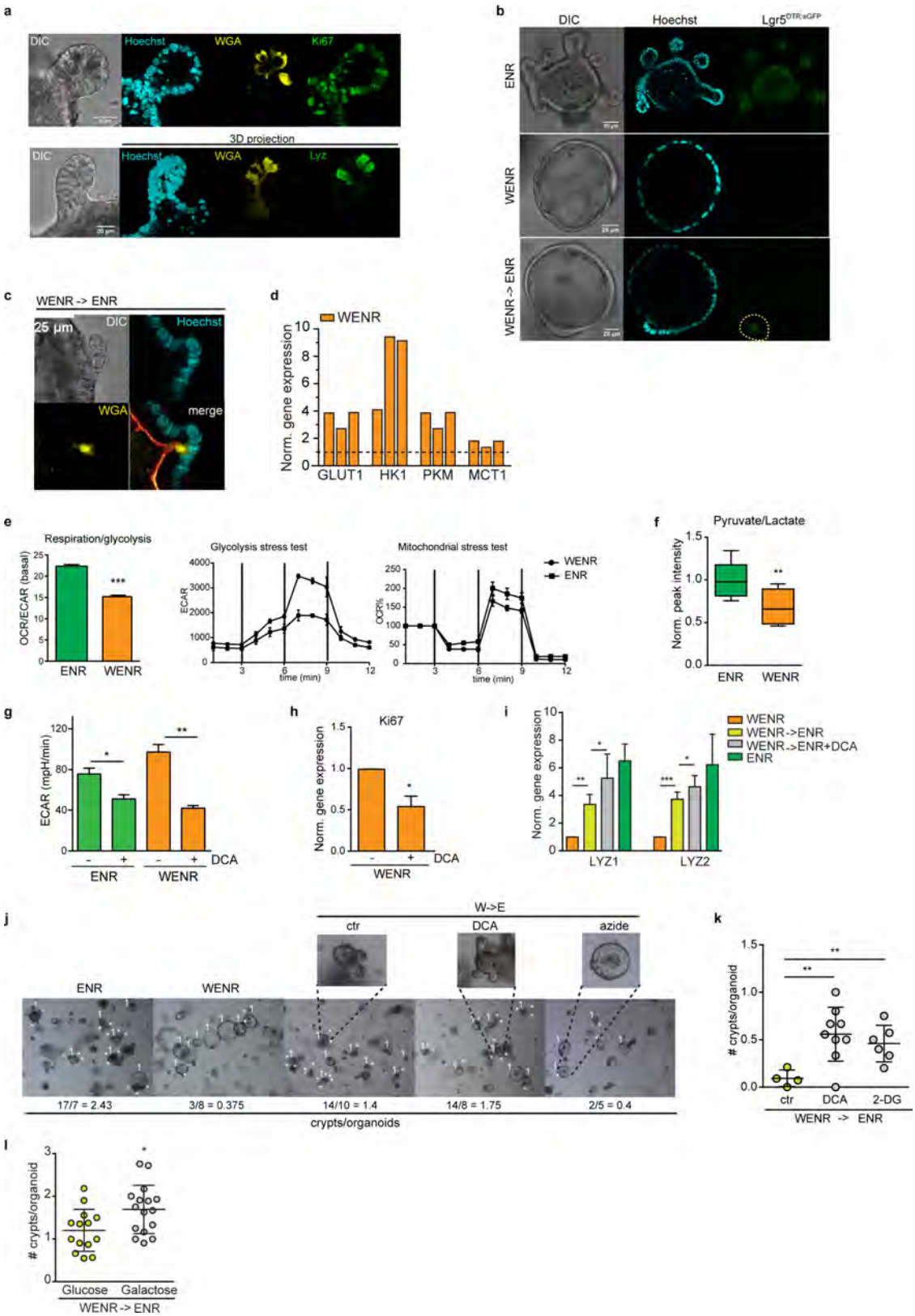

Extended Data Figure 2 | See next page for caption.

Extended Data Figure 2 | WENR organoids represent a homogeneous population of glycolytic dividing cells that retain pluripotency. **a**, Confocal images of organoid crypts. PC and nuclei were detected using WGA or Lyz antibody, and Hoechst, respectively. *z*-stacks are represented as 3D projections. **b**, Confocal live imaging of DTR–Lgr5–eGFP-derived mouse organoids. $Lgr5^{+}$ cells are visualized in green. Dashed yellow region indicates a bud structure that constitutes a starting crypt. **c**, Confocal microscopy of immunostaining of an emerging crypt. Phalloidin was used to stain F-actin (in red) ($n = 3$ (**a**–**c**)). **d**, Gene expression of glycolytic genes in WENR organoids normalized by the expression in ENR organoids (dashed line) ($n = 3$). **e**, Bioenergetics was determined by Seahorse technology. Results show one representative experiment of 3 independent ones. **f**, Pyruvate/lactate ratio was analysed by DIMS metabolomics. Boxes and error bars correspond to mean and s.d. of 3 technical replicates of 3 biological samples. **g**, DCA inhibition of glycolysis in ENR or WENR grown organoids was determined by Seahorse technology 1 representative experiment of $n = 3$. **h**, Proliferation was measured by Ki67 gene expression by qPCR. **i**, Gene expression of PC markers ($n = 5$ independent experiments). **j**, Representative images of a differentiation assay and the effect of DCA and azide; spherical organoids (grown in WENR) forming crypts (WENR→ENR) and cryptic organoids (grown in ENR medium). **k**, Effect of glycolysis inhibition on crypt formation was analysed by differentiation assay using DCA or 2-deoxyglucose (one representative experiment, $n = 2$). **l**, Increased crypt formation by activation of mitochondria (**h**) was analysed by differentiation assay replacing glucose by galactose in ENR medium. Two-tailed *t*-test, $***P < 0.001$; $**P < 0.01$; $*P < 0.05$.

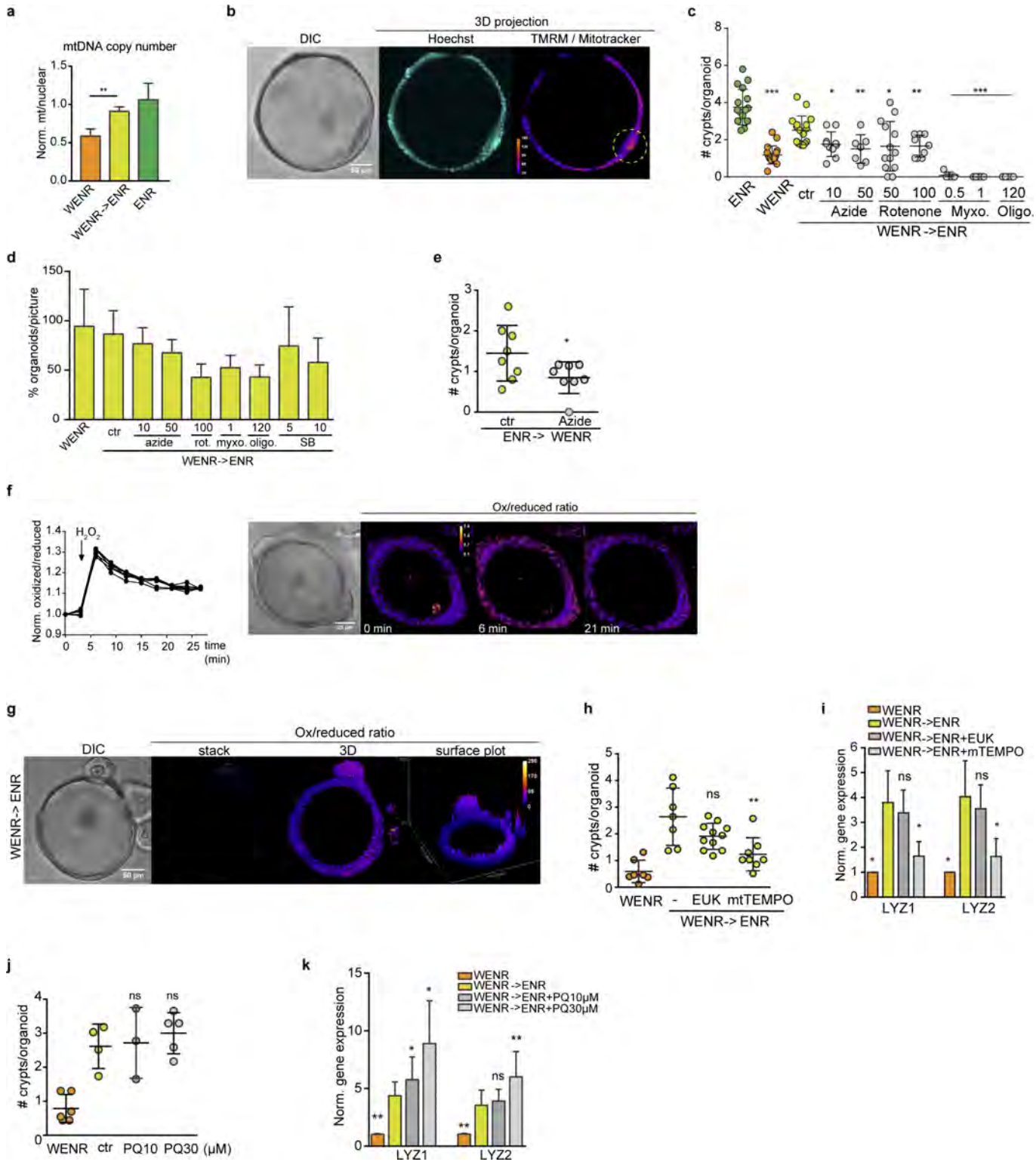

Extended Data Figure 3 | See next page for caption.

Extended Data Figure 3 | Mitochondrial OXPHOS and ROS signalling drive differentiation and crypt formation. a, Mitochondrial DNA copy number was quantified by qPCR on total DNA. Plot represents one representative experiment ($n = 2$). **b**, Mitochondrial membrane potential and total mitochondria were analysed with the combination of Mitotracker Deep Red (mitochondria) and TMRM (mitochondrial membrane potential). Staining is represented as a ratio using fire intensity scale (ImageJ). Dashed yellow region indicates a bud structure that constitutes a starting crypt. **c**, Decreased crypt formation by inhibition of mitochondria was analysed by differentiation assay adding OXPHOS inhibitors: azide, myxothiazol (myxo.), rotenone and oligomycin (oligo.) (concentrations in μM). **d**, Toxicity of OXPHOS inhibitors was measured by counting the number of organoids growing in the depicted conditions. Values are plotted as percentages of the WENR condition (mean). **e**, Mitochondrial inhibition enhances inhibition of crypt formation occurring when plating ENR organoids in WENR medium. Azide (50 μM) was added to the medium, pictures were taken after 48 h and the number of crypts per organoid was counted using ImageJ. Average and s.d. are shown. Representative of one experiment ($n = 2$). **f**, The sensitivity to redox changes of the mtGrx1–roGFP in organoids was analysed by live imaging, applying 500 μM hydrogen peroxide and following the redox response in time. Images represent the ratio of oxidized/reduced sensor. **g**, Mitochondria redox state of a forming crypt was assessed by live imaging of mtGrx1–roGFP. **h**, **i**, Effect of ROS scavengers on crypt formation was analysed by differentiation assay (**h**) and Paneth cell markers gene expression (**i**) in the presence of EUK134 (5 μM) and mitoTEMPO (0.5 mM). **j**, **k**, The effect of triggering mitochondrial ROS on crypt formation was performed by differentiation assays applying paraquat and counting the number of crypts per organoids (**j**) and by the expression of Paneth cell markers by qPCR (**k**). One representative experiment of $n = 3$ (**c**, **d**) or $n = 5$ (**h**, **j**). Mean and s.d. are shown. Two tailed *t*-test; asterisks or NS indicate comparison to WENR→ENR control, * $P < 0.05$, ** $P < 0.01$.

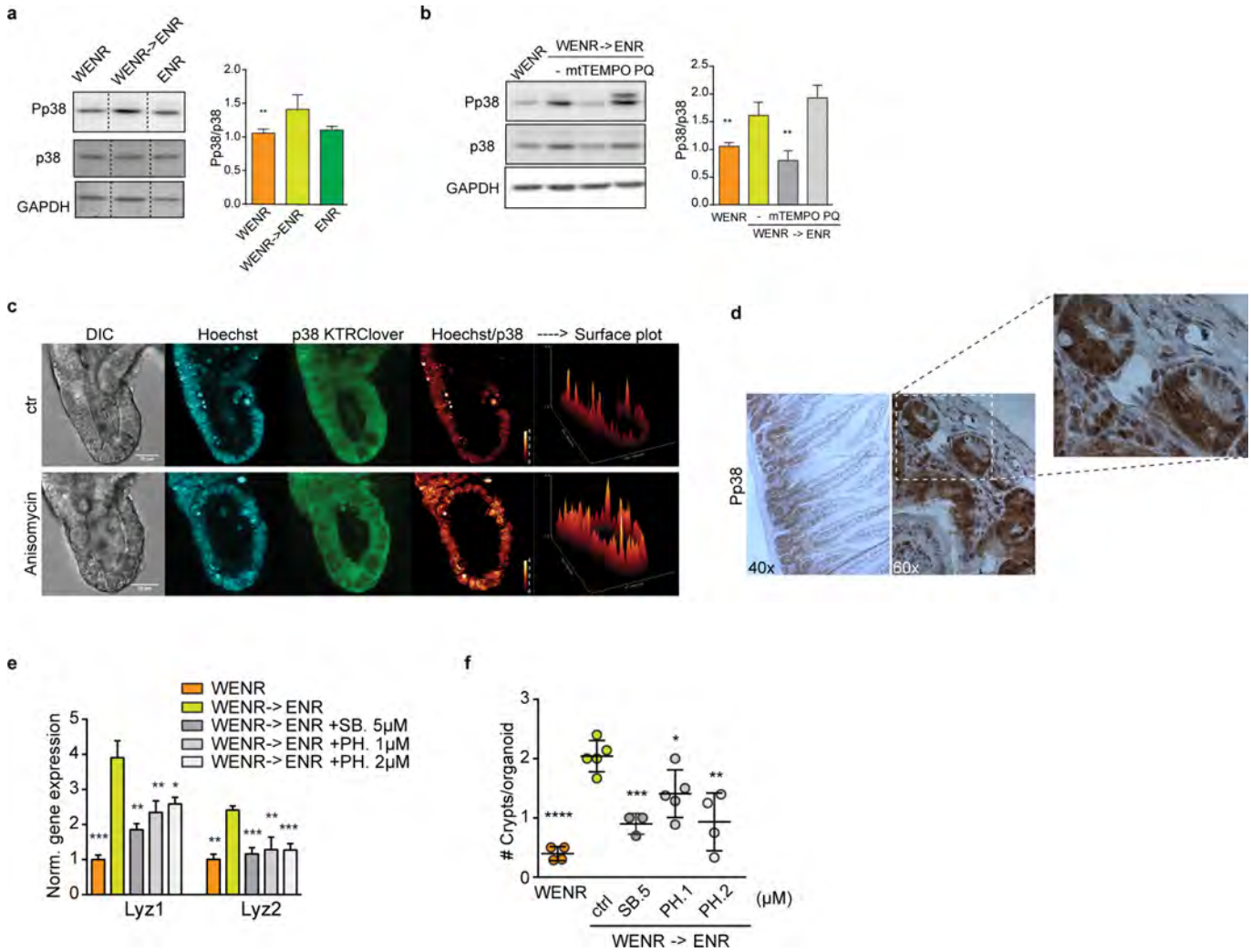

Extended Data Figure 4 | p38 activity drives differentiation and crypt formation in a mitochondrial ROS signalling dependent manner. **a**, **b**, P38 activation was analysed by western blot and quantified. For gel source data see Supplementary Fig. 1. Organoids were treated with mitoTEMPO (0.5 mM overnight) or paraquat (7.5 mM, 1.5 h) ($n = 3$) (**b**). **c**, p38KTRClover organoids were challenged with anisomycin (75 µg ml^{-1}) in order to analyse p38 activity. Images were obtained during 45 min after the addition of the compound. *z*-stacks of p38KTRClover or Hoechst/p38KTRClover ratio are represented as 3D projections and surface plot of 3D projections. Ratios are represented in either fire or real glow scale (ImageJ). **d**, Immunohistochemistry of p38 on mouse intestinal sections. **e**, **f**, Decreased differentiation and crypt formation upon p38 inhibition was analysed by differentiation assays (one representative experiment of $n = 5$) (**e**) and gene expression of *Lyz1* and *Lyz2* (**f**) in the presence of p38 inhibitors SB203580 and PH-797804. Mean and s.d. are shown ($n = 5$). Asterisks indicate comparison to WENR→ENR control; two-tailed paired *t*-test, $*P < 0.05$, $**P < 0.01$, $***P < 0.001$ and $****P < 0.0001$.

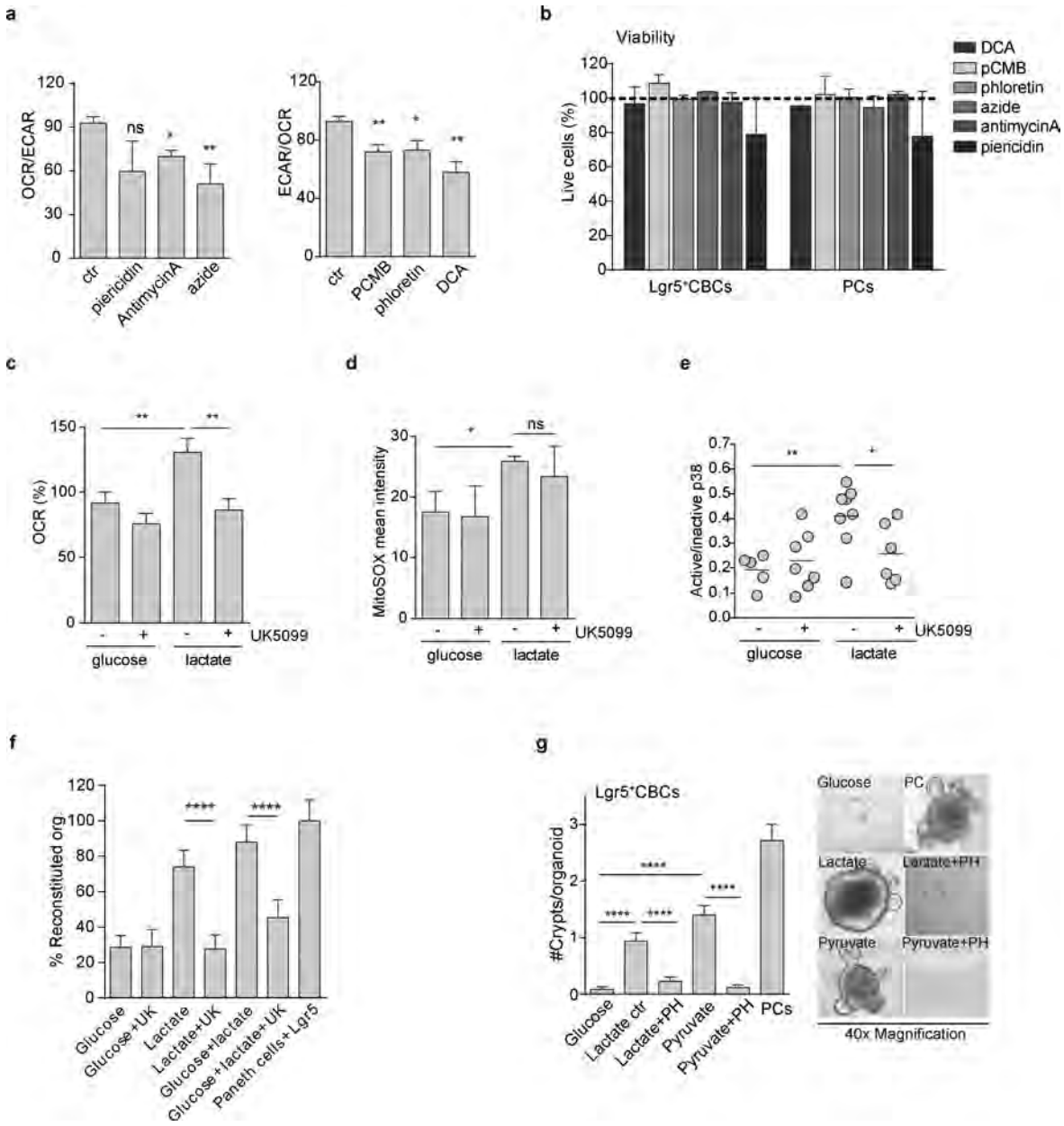

Extended Data Figure 5 | Mitochondrial activity, mitochondria ROS signalling and p38 activity regulate stem cell function of Lgr5$^+$ CBCs. **a**, The effects of the indicated compounds on respiration and glycolysis were tested after 3 h of the treatments using mitochondrial stress test (Seahorse technology). Bars and error bars represent the mean of the basal ratios and s.e.m. of 4 independent experiments with 4 technical replicates each. **b**, Cell viability after mitochondria and glycolysis inhibition treatments on CBCs and Paneth cells. Primary intestinal Lgr5$^+$ CBCs and Paneth cells were treated with the indicated compounds for 2 h and then washed and stained with PI before FACS. PI negative and positive cells were counted as alive and dead, respectively. Values are plotted as percentages of the untreated cells (100%) indicated as a dashed line. Mean and s.d. of 2 independent experiments with 2 technical replicates each are represented in the graph. **c**, Effect of lactate and inhibition of pyruvate mitochondrial transport on mitochondrial respiration. Maximal respiration was measured by performing mitochondrial stress test after two hours of incubation with glucose or lactate with or without UK5099. Mean and s.d. are shown of 3 independent experiments with 4 technical replicates in each. **d**, Effect of lactate and inhibition of pyruvate mitochondrial transport on mitochondrial superoxide production. Mitochondrial superoxide was measured by FACS analysis of single cells stained with MitoSOX after 2 h of incubation with the indicated compounds. The graph represents the mean and s.d. of 4 independent experiments. **e**, P38 activity was monitored in p38KTRClover organoids growing for three days in the indicated conditions. P38 activity is measured by the ratio of cells with active (cytosolic localization)/inactive (nuclear localization) of the signal. The graph shows the counting of one representative experiment of 3 independent ones and each dot represents one organoid. **f**, The effect of inhibition of pyruvate transport to mitochondria on stem cell function was measured as number of reconstituted organoids from primary Lgr5$^+$ CBCs in the depicted conditions. The graph represent the mean and s.d. of 3 independent experiments. Two-tailed *t*-test, $*P < 0.05$, $**P < 0.01$, $***P < 0.001$. **g**, Number of crypts per reconstituted organoid and representative images of the referred conditions. The plot represents mean and s.e.m. of 35 organoids of one representative experiment of $n = 6$. Mann–Whitney test, $****P < 0.0001$. In **a**, **c**–**e**, organoids were grown on ENR, CHIR99021 and valproic acid to enrich them with stem cells and the experiments were performed on single cells after trypsinization. In **b**, **f**, **g**, experiments were performed in mouse intestinal crypt FACS-sorted cells.